Geochemical and mineralogical characterization of streams and wetlands downstream a former uranium mine (Rophin, France)

Sylvain Grangeon, Céline Roux, Catherine Lerouge, Patrick Chardon, Romain Beuzeval, Gilles F Montavon, Francis Claret, Thomas Grangeon

Applied Geochemistry 150 (2023) 105586

Contents lists available at ScienceDirect

Applied Geochemistry

journal homepage: www.elsevier.com/locate/apgeochem

Geochemical and mineralogical characterization of streams and wetlands downstream a former uranium mine (Rophin, France)

Sylvain Grangeon [a,*], Céline Roux [a,b], Catherine Lerouge [a], Patrick Chardon [b,c], Romain Beuzeval [b], Gilles Montavon [b,d,**], Francis Claret [a], Thomas Grangeon [a]

[a] BRGM, 3, Avenue Claude Guillemin, 45060, Orléans, cedex 2, France
[b] SUBATECH, UMR 6457 (IMT-Atlantique, Université de Nantes, CNRS-IN2P3), 4 Rue Alfred Kastler, 44307, Nantes, France
[c] LPC, UMR 6533, 63170, Aubière, France
[d] LTSER "Zone Atelier Territoires Uranifères", 63000, Clermont-Ferrand, France

ARTICLE INFO

Editorial handling by: Dr C S Eckley

Keywords:
Uranium
Sequential extraction
Selective extraction
Uranium mines
Radiological mapping
Sediment
Soil
Trace elements
Technosols
Histosols

ABSTRACT

The geochemical distribution of U and associated major and trace elements (As, Li, Pb, Sr, Zn) was studied at the former Rophin U mine (Puy-de-Dôme, France). Three zones of contrasting radiological settings were identified and sampled: a background area (<200 nSv·h^{-1}), a streambed flowing downstream of the former mine (radiation level between 200 and 800 nSv·h^{-1}) and a wetland soil (>1000 nSv·h^{-1}). Sediment and water samples were collected both in a streambed located in the background area and in the streambed downslope the former mining area, and a soil sample was collected in the wetland downslope. Using both sequential and selective chemical extractions, and quantifying also the chemical reservoirs of As, Li, Pb, Sr, and Zn, it could be concluded that, in the streams, U was mainly bounded to primary ore minerals (phosphates) that were transported through particulate transport. It was also bound, to a lower extent, to clays, Mn oxyhydroxides and organic matter, certainly due to the sorption of aqueous U originating from partial dissolution or leaching of primary ore materials. Ore minerals remaining stable in the stream sediments were certainly included in a quartz matrix and hence were not in accessible for dissolution. In the wetland soil, selective extractions evidenced that U was about evenly distributed between humid/fulvic acids and organic matter unaffected by NH_4OH 1M.

1. Introduction

Decades of uranium (U) mining and milling in France have left a legacy of environmental liabilities (Barescut et al., 2005). Mill tailing waste, former mines, or remaining ore bodies (in contact to the atmosphere or flooded), could represent a source term of chronical U discharge. In nearby areas, living organisms could be exposed to radionuclides (RN) such as U by two processes: radiation from radioactive decay and chemical toxicity following RN uptake (Møller and Mousseau, 2011). This second process is considered to be more impactful (Minouflet et al., 2005) and is directly related to RN bioavailability and thus to the chemical speciation (Bresson et al., 2011; Salbu, 2007), itself depending on local geochemical parameters. The study of U biogeochemical cycle in RN-enriched environments, for example former U mines, is important to the understanding of both RN speciation in the geosphere and of RN interaction with the biosphere.

Previous studies of former U mines have shown an increase in gamma radiations compared to the local geochemical background and U concentrations reaching hundreds of μg·g^{-1}, resulting in potential environmental threats (Bermudez et al., 2010; Bister et al., 2015; Boekhout et al., 2015; Cuvier et al., 2015; Lind et al., 2013; Neiva et al., 2014; Salbu et al., 2013). In groundwater, U concentrations up to several tens of mmol·L^{-1} were measured (Lottermoser and Ashley, 2005; Pinto et al., 2004; Salbu et al., 2013), whereas drinkable water should not contain more than 7 mmol·L^{-1} U (WHO, 2004). Neiva et al. (2014) investigated the specific case of streams under influence of former Portuguese U mines, where a mineralized quartz vein from a granitic rock contains uranium under the form of autunite, tobernite, uraninite, meta-tobernite, sabugalite, parsonite, phosphuranylite, and black uranium oxides. Excluding low pH (<3) and high-sulfate (>1000 μg·L^{-1}) waters, indicative of leaching from sulfur-bearing minerals that can induce acid mine drainage, stream pH ranged between 5 and 8, HCO_3^-

* Corresponding author.
** Corresponding author. SUBATECH, UMR 6457 (IMT-Atlantique, Université de Nantes, CNRS-IN2P3), 4 Rue Alfred Kastler, 44307, Nantes, France.
E-mail addresses: s.grangeon@brgm.fr (S. Grangeon), montavon@subatech.in2p3.fr (G. Montavon).

https://doi.org/10.1016/j.apgeochem.2023.105586
Received 11 July 2022; Received in revised form 14 January 2023; Accepted 23 January 2023
Available online 28 January 2023

was the main anion (concentration comprised between 1 and 21 $mg{\cdot}L^{-1}$), and Na^{+} was the main cation (concentration comprised between 4 and 9 $mg{\cdot}L^{-1}$). Aqueous U concentration ranged between 30 and 75 $\mu g{\cdot}L^{-1}$ and geochemical calculations suggested that, under such geochemical conditions, aqueous U was under the +6 oxidation state and complexed to carbonate ions. However, in streams, U is transported not only as a dissolved species, but can also be subject to colloidal (particulate) transport (Pinto et al., 2004), with the relative proportion of each mechanism depending on different factors such as stream flow.

Here, we investigated the Rophin site, located downstream a former U mine, in the French Hercynian belt where many metallic deposits were exploited (Sb, Au, Ag, Pb, Sn, Ba, Zn, W, U - Ballouard et al., 2018; Bouchot et al., 2005; Bril et al., 1994; Marignac and Cuney, 1999; Romer and Cuney, 2018). The main objective was to determine the mechanisms responsible for U migration within a stream located downstream the tailings of the former mine, including the relative importance of particulate transport and sorption of aqueous U by mineral phases. First, we determined the radiological background of the study site and the area having anomalously high radiological state. Then, in several stream water and sediment samples, the geochemistry of U and of other trace elements of interest (As, Ba, Li, Pb, Sr, Zn) was studied, and the mineralogical reservoirs were identified. Finally, the possible uptake of U by the living was studied through the study of U distribution in a wetland, which is located downstream the Rophin site and which was previously studied by Martin and coworkers (Martin et al., 2020, 2021). These authors could demonstrate that the wetland soil profile is composed of three main horizons: the first one, referred to as "black soil", extends from the surface to 10–15 cm depth, and is mainly made of organic matter (about 50%), with presence of fibrous material and roots. Its ^{238}U content increases with depth, from about 100 $mg{\cdot}g^{-1}$ to about 1800 $mg{\cdot}g^{-1}$. In the second horizon ("white soil"), which has low (8%) organic matter content and a silt loam texture, ^{238}U concentration first decreases down to 600 $mg{\cdot}g^{-1}$ at mid-depth of the horizon, and then increases up to about 3500 $mg{\cdot}g^{-1}$ at the bottom of the horizon, which is located at 20–30 cm depth. Finally, the third horizon ("brown soil"), which extends down to about 70 cm depth, ^{238}U concentration is lower than in the two other horizons, with a mean value of about 250 $mg{\cdot}g^{-1}$. The white loam horizon originates from deposition of mining materials, possibly during a flooding event. In the black soil, developed on the white horizon, ^{238}U is adsorbed to Mn/Fe oxyhydroxides and to organic matter, with organic matter being the main reservoir. However, the nature of the organic matter reservoir (fresh or humified) was not elucidated. Such information is however important to the determination of the retention mechanisms (sorption of aqueous U onto humidified organic matter or U uptake by the living).

Overall, this study, based on a multi-technique approach, will provide baseline data for future studies aiming at understanding, and thus ultimately predicting and modeling U reactivity in the environment. Indeed, such modeling work requires a sound description of the whole geochemical system, including distribution of the elements of interest between the different mineralogical phases (Poinssot and Geckeis, 2015).

2. Site statement

The Rophin ICPE ("classified installation for the protection of the environment") is one of the 17 sites for the storage of U wastes in France (Barescut et al., 2005). It is located in the Forez massif, east of Limagne graben (Fig. 1). It is a former U mining area where mill tailing waste has been stored *in situ* after exploitation closure (1957) and where the living has freely evolved since (Himeur, 2010). Its ore mineralogy strongly resembles that of the study by Neiva et al. (2014), *i.e.* autunite-bearing granite. The storage site is located in a 98 ha headwater catchment, mainly covered with forested area and grassland. It is tributary to the Allier River, located within the Loire River basin.

A 50-cm resolution LiDAR digital elevation model was acquired

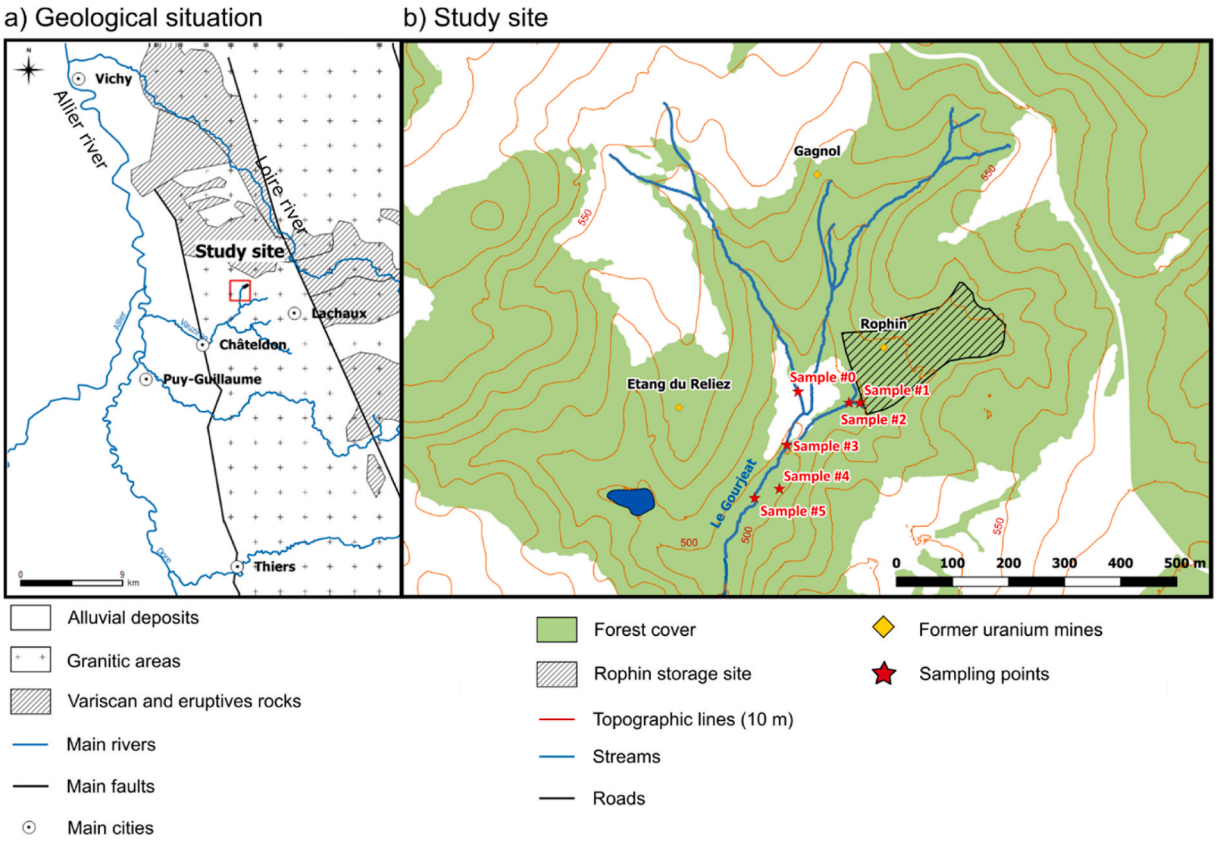

Fig. 1. (a): Rophin site localization and geological context and (b) detailed view of the study site.

during winter 2017–2018. In the catchment, elevations are ranging from 492 m to 615 m, with steep slopes in the upper part of the catchment and flatter zones near the Gourjeat River. Accordingly, the streambed slope was high near the storage site, ranging between 5% and 20% (mean: 13%). Downstream, the slope decreased significantly and was ranging between 0% and 10% (mean: 3%).

The ore body was discovered in 1924 and was first exploited for Ra, then for U from 1948 to 1952. In the vicinity, four other ore bodies were exploited (Himeur, 2010): Gagnol (1949–1953 - Fig. 1), Etang du Reliez (1951–1953), Reliez (1949–1952) and Bancherelle (1952–1954). In the Lachaux sector, U ore occurs as lodes hosted by coarse-grained peraluminous alkaline granite, emplaced at the end of Hercynian orogeny. The Rophin lode, in the continuity with the Etang de Reliez lode, is a 700 m long and thick lode deeping to the west. It is oxidized and consists of low-temperature silica and quartz with parsonite [$Pb_2(UO_2)(PO_4)_2{\cdot}2H_2O$] and autunite [$Ca(UO_2)_2(PO_4)_2{\cdot}nH_2O$] (Himeur, 2010). About 400 kg U were extracted from an ore mean concentration of 2‰ (Barescut et al., 2005), using a mechanical ore washing plant, built in 1948. Ore treatment was first gravimetric with a vibrating table, crushing machines and a flotation circuit. In 1953, a chemical ore washing procedure was tested, using pressurized Na_2CO_3. After exploitation closure, 30 000 tons of mine and mill tailing waste were stored at the former Rophin mine (hatched area in Fig. 1b) (Himeur, 2010).

A vegetated belt dam of tailings and waste stabilizes the wastes, and vegetation has developed at the top of the mine waste storage (Himeur, 2010). A drain collects upstream water and deviates it to avoid contact with the storage site. A stream flows downstream of the storage site and mixes with the Gourjeat stream (Fig. 1). Twice a year, U concentration is analyzed in water samples. In the stream located downstream the storage site, U concentration was reported to range between about 0.01 and 0.03 $\mu mol{\cdot}L^{-1}$ (Himeur, 2010; Meyer-Georg, 2021).

3. Material and methods

3.1. Mapping

The radiological mapping was set up focusing downstream the former U site. A gamma ray map was built using a gamma-ray sensor equipped with a ICTO device (Carmelec inc.), a GPS (Trimble inc.), and a gamma-ray sensor coupled with a Colibri device (Canberra inc.). Data were acquired at 90 cm above the ground. With the first device, data were acquired manually, every 2–5 m. With the second one, data were acquired automatically every 30 s. All data, collected in December 2014 and August 2015 were consistent and were merged to build a dataset of 5974 points. Soil and sediment sampling strategy was elaborated based on this radiological mapping (see below).

3.2. Sampling

Both water, sediment and soil samples were collected (Fig. 1b). Water and sediment samples were collected in two streambeds, belonging to (i) a stream considered as non-influenced by the Rophin site (sample #0), and (ii) in a stream, located just downstream of the ICPE, that possibly collects water from the drain described above. In this second stream, samples were collected just below the mill tailing storage site (sample #1) and downstream, where red precipitates were observed (sample #2). Sample #3 was collected at the confluence of the two streams (sample #3), and sample #5 was collected downstream the confluence. Finally, a soil surface sample (sample #4) was collected in a wetland that was previously analyzed, in particular for its U concentration as a function of depth (Martin et al., 2020).

A preliminary sediment sampling was performed at location #1 (Fig. 1) in December 2014 to determine the most adequate method for major and trace elements quantification (see below). In June 2015, sediment and stream water samples were collected at sampling locations #0, #1, #2, #3 and #5. In addition, sample #4 was collected in the first centimeters of the radiologically marked wetland soil to complement results obtained by Martin and coworkers (Martin et al., 2020, 2021). To avoid alteration, solids were stored in liquid N_2 until analysis. Stream water samples were filtered *in situ* (cut-off diameter of 0.45 μm). Aliquots of 50 mL were stored without any further conditioning and used for quantification of Cl^- and SO_4^{2-}. Another 50 mL aliquots were acidified with HNO_3 and used for quantification of cations (Na^+, K^+, Ca^{2+}, Mg^{2+}), Si, and trace elements (e.g. Fe, Mn, U). Geochemical parameters (pH, redox potential, temperature, conductivity, dissolved O_2) were measured *in situ* with a CyberScan PCD 650 multimeter and CyberScan pH 110 m coupled with a redox sensor (Eutech instruments inc.). NO_3^- quantification was attempted *in situ* with a Merck (inc.) kit, but was systematically below the detection limit. Alkalinity was titrated *in situ* and less than 1 h after sampling with a colorimetric technic, using phenolphthalein ($C_{20}H_{14}O_4$) and HCl.

3.3. Laboratory analyses

3.3.1. Radiological analyses

Sediments were crushed, dried at 100 °C for 48 h, and weighted before and after drying to quantify their water content. Gamma activities were counted for 50 000 s using HPGe-detectors (Canberra, BE4823/S, Ge-crystal, 7500SL cryostat, 2002CPSL pre-amplifier) and a multi-channel analyzer (MCA). Counting results were treated following the NF EN ISO 18589-3 guidelines.

3.3.2. Chemical and mineralogical analyses on solid samples

3.3.2.1. Samples preparation. In the laboratory, solid samples that were initially stored in liquid N_2 were freeze-dried and then divided in three aliquots used respectively for granulometric, chemical, and mineralogical analyses.

3.3.2.2. Total chemistry. Major and trace elements in the sample collected in 2014 were measured by X-ray fluorescence. Since the Na content was found to be low (1.9 wt percent – wt% Na_2O), it was decided to analyze all samples collected in 2015 by ICP-MS after sample digestion by alkaline fusion. The use of alkaline fusion prevented Na quantification but allowed for a more precise quantification of all other elements. C and S were quantified by combustion infrared detection technique (LECO analyzer).

3.3.2.3. X-ray diffraction. Powder X-ray diffraction (XRD) was carried out on randomly oriented bulk powder sediment using a SIEMENS D5000 X-ray diffractometer operating at 40 kV and 30 mA and equipped with Co Kα anode ($\lambda = 1.789$ Å). Data were acquired in the 4–84 °2θ interval, with a 0.04 °2θ step size and 18 s counting time per step. Quantification was performed using the Profex interface to BGMN (Doebelin and Kleeberg, 2015). Clay mineralogy was further investigated by recording the XRD pattern of oriented <2 μm powders, successively in air-dried and ethylene glycol conditions, using the same diffractometer, the same Co anode, in continuous scan mode, and in the 4–38 °2θ interval, with a 0.02 °2θ step size and 4 s counting time per step. Note that the amount of sample used for extraction of the <2 μm fraction could not be strictly controlled due to low sample quantity. Hence, the intensity of the 00*l* reflections in the XRD patterns of the oriented powders cannot be used to estimate relative mineral abundances between samples, in particular in such samples that have very low concentration of clay minerals.

3.3.2.4. Microscopy. Dry bulk sediments and < 2 mm, <0.5 mm, and <0.08 mm granulometric fractions were embedded in Araldite resin and mounted in thin polished sections. Optical observations were performed using an Olympus BH2 microscope under transmitted and reflected lights. The size of mineral grains and particles were measured under the

microscope using the Archimed® software calibrated with a micrometer. Complementary observations and analyzes were performed using a TESCAN MIRA 3 XMU FE scanning electron microscope (SEM) coupled with an energy dispersive X-ray spectroscopy (EDS) detector (EDAX, USA) and a APOLLO XPP silicon drift detector. Prior to analysis, a thin carbon layer was sputter-coated on the samples.

3.3.2.5. Loss on ignition. Loss on ignition experiments were performed to quantify organic matter (O.M.) content. For this purpose, samples were heated successively at 105 °C overnight and at 550 °C for 5 h. At the beginning of and after each step, samples were cooled to room temperature in a desiccator and then weighted.

O.M. content (in w%) was calculated according to Eq. (1):

$$O.M. = \frac{W(105°C) - W(550°C)}{W(105°C) - CW} * 100 \quad \text{Eq. 1}$$

Where CW, W(105 °C), and W(550 °C) respectively are the weight of the empty crucible and the weight of the sample plus crucible after heating at 105 °C and 550 °C.

3.3.3. Stream water samples

Anion (Cl^-, SO_4^{2-}) and cations (Na^+, K^+, Ca^{2+}, Mg^{2+}) were quantified by ionic chromatography (Dionex inc. And Metrohm inc.). As, Ba, Li, Pb, Sr, U, Zn were quantified by Inducted Coupled Plasma Mass Spectrometry (ICP-MS XSERIES 2, ThermoFisher Scientific inc.) and Si and Fe in collision chamber mode (addition of H/He) by ICP-MS. Samples were diluted in a 2% HNO_3 solution when needed.

3.3.4. Sequential and selective extraction procedures

Sequential extractions were performed on sediment samples (#0, #1, #2, #3, #5), following Claret et al. (2010) and Grangeon et al. (2015), themselves based on Tessier et al. (1979) and Gatehouse et al. (1977). This protocol extracts chemical reservoirs in targeting mineralogical phases (Table 1). The justification for the phases that were targeted at each step, and a discussion about potential non-selectivity or overlaps is provided in the following.

The sequential extraction procedure (Table 1) started by weighting ~1 g aliquots of crushed samples and introducing them in polysulfone centrifuge cones. In the first step, samples were put overnight in contact with 20 mL of degassed ultrapure water (resistivity = 18.2 Ω·cm) in a glove box with N_2 atmosphere. After this step, and as for all subsequent extraction steps, liquid and solid phases were separated by centrifugation (20 °C, 20 min, 4500 rpm), the liquid phase was filtered (cut-off diameter of 0.1 μm), and both extracted liquid phase and remaining solid (including solution remaining in the porosity) were weighted. Then, 20 mL of 1 M ammonium acetate solution was added to the tubes, which were agitated for 24 h. In a third step, solids were contacted for 6 h with a 20 mL 1 M ammonium acetate solution buffered at pH 5 with acetic acid. In a fourth step, solids were contacted with 20 mL of a 0.04 M hydrochloride hydroxylamine solution for 24 h. Finally, a 30% H_2O_2 solution, adjusted to pH 2 with HNO_3, was added to the solid and heated to 85 °C until all H_2O_2-reducible material was dissolved. 5 mL of 3.2 M ammonium acetate solution was added to the solution to avoid any readsorption reaction. After the last extraction step, solids were freeze-dried and weighted. Two experiments were also done with the same procedure but without solids to quantify the contamination at each step.

A selective extraction procedure was applied to soil sample #4 to quantify elements associated to fresh and developed organic matter (Table 1). First, the solid was contacted with 20 mL of a 1 M NH_4OH solution for 1 h (Di Giulio and Ryan, 1987; Guedron et al., 2009; Williams et al., 1996) to extract humified organic matter (humic and fulvic acids). After solid/liquid separation, the solid was contacted with a 30% H_2O_2 solution at pH 2 and at 80 °C. This second step allowed extracting components of higher molecular weight, and in particular lignin, unaffected by NH_4OH (Zhu et al., 2012) and assumed representative of non- or low-degraded organic matter (hereafter referred to as "fresh organic matter"). The experimental protocol was identical to that of the sequential extraction.

Since no preliminary extraction step was performed, NH_4OH also possibly extracted water-soluble elements and those associated to clay interlayer. However, Martin and coworkers (Martin et al., 2020, 2021) could demonstrate that U is, in the studied wetland, mainly associated to organic matter and, to a lesser extent, to Mn/Fe oxides. In addition, NH_4OH does not extract significantly Mn/Fe oxides (Breward and Peachey, 1983). Hence, it was assumed that the interpretation of data obtained with the present protocol is not biased by extraction of non-targeted U-bearing phases.

The concentration of the element of interest, determined with the same methodology as stream water samples and extracted at any step, was calculated as (Eq. (2)):

$$C_{solid} = 10^6 \times M \times \frac{\left(C_i - C_{blank}\right) \times V_i - C_{i-1} \times \left[m_{sol,i-1} - \left(m_{i,i-1} - m_{f,i-1}\right)\right]}{m_{sample}} \quad \text{Eq. 2}$$

where C_{solid} is the concentration, in the solid phase, extracted at a given i^{th} step, M is the molar mass of the element of interest, C_i and C_{i-1} are the concentrations in the liquid phase at the i^{th} and $(i\text{-}1)^{th}$ step, $m_{i,i-1}$, $m_{f,i-1}$, and $m_{sol,i-1}$ are respectively the masses (tubing + sample + liquid) before and after the liquid phase is discarded and the mass of reactant added at the $(i\text{-}1)^{th}$ step ($i \geq 1$), V_i is the volume of the reactant used (determined by weighting), C_{blank} is the concentration of the element of interest measured in the blank experiment at the step i, and m_{sample} is the mass of the sample used for the experiment. All concentrations are in $mol \cdot L^{-1}$ except C_{solid} ($\mu g \cdot g^{-1}$), volumes are in L, and masses in kg, except m_{sample} (g). A principal component analysis was performed with the PAST software (Hammer et al., 2001).

3.3.5. Enrichment factors calculations

Enrichment factors (EF; Eq. (3)) quantify the percentage of gain or loss, in the solid phase, of a mobile element relative to a refractory one, according to Guédron et al. (2013; 2006):

$$EF = 100 \times \left(\frac{[j]_s}{[i]_s} \times \frac{[i]_p}{[j]_p} - 1\right) \quad \text{Eq. 3}$$

Where i and j are respectively the refractory (here, Ti) and mobile

Table 1
Reagents, contact times, and target phases for all steps of the sequential and selective extraction procedures.

Procedure	Step	Reagent	Time	Target
Sequential extraction	1	H_2O	over night	Soluble phases
	2	CH_3COONH_4 1 M	24 h	Clay interlayer
	3	CH_3COONH_4 1 M at pH 5	6 h	Phosphates (partially)
	4	$NH_2OH{\cdot}HCl$	24 h	Fe/Mn oxyhydroxides
	5	H_2O_2 + HNO_3		Organic matter
Organic matter extraction	1	NH_4OH 1 M	1 h	Humic and fulvic acids ("developed organic matter")
	2	H_2O_2 + HNO_3		Lignin ("fresh organic matter")

elements, and subscripts *s* and *p* refer to the concentration of each element in the considered sample and in the sample assumed to be representative of the parent sediment (here, sample #0), respectively.

4. Results and discussion

4.1. Gamma cartography

Three radiological zones were identified (Fig. 2a): (i) an area of local geochemical background that contained a stream, with radioactivity <200 nSv·h^{-1} (≈150 c·s^{-1}; white to light pink in Fig. 2a), (ii) a second stream downstream the ICPE, with radioactivity in the streambed ranging 200–800 nSv·h^{-1} (light to dark pink in Fig. 2a), and (iii) a wetland located S/SE of confluence, with radioactivity >1000 nSv·h^{-1} (≈1000 c·s^{-1}, light to dark red in Fig. 2a). This preliminary analysis was used to determine sampling strategy for soils and sediments. Sediment samples were collected (Fig. 2a) in the streambed having background radiological values (sample #0), in the radiologically marked streambed (samples #1, #2, #3, #5) and in the radiologically marked wetland (sample #4).

4.2. Stream water samples

The geochemical data of all stream water samples is reported in Table 2.

The pH value of the stream water collected just downslope the ICPE (point #1) was 6.0, and increased to 6.9–7 downstream (points #2 and #3). After the stream water was mixed with the one that in the geochemical background area (point #0; pH = 5.2), the resulting pH was intermediate (6.4; point #5). Major elements are displayed as Piper (Fig. 3a) and Stiff (Fig. 3b) diagrams while trace element concentrations were often lower than the detection limit, and no relation could be made with chemical parameters or position in the stream.

All stream waters felt into the mixed-type bicarbonate profile. They are compared in Fig. 3 to waters hydrologically connected to the study site, namely rainwater (Mohammed et al., 2014), Allier River and Dore River, both close to the outlet of the study site (Naiades database; Mohammed et al. (2014)), and an affluent of Allier River in a granitic bedrock (Malaval river; Steinmann & Stille (2008)). As for pH values, geochemical composition of the stream water collected at point #5 was generally intermediate between that of points #2/#3 and #0, coherent with a mixing of the two streams near point #3. Point #2 stream water alkalinity and Ca concentration were higher than that of the four other stream waters. Because calcite was undersaturated and never observed,

Table 2
Geochemistry of the stream water samples. Numbers under brackets are the uncertainty on the last digit and < Q.L. stands for "below the quantification limit".

Parameter	Sampling point				
	Point #0	Point #1	Point #2	Point #3	Point #5
Chemical parameters					
pH	5.2	6.0	6.9	7.0	6.4
Conductivity (µS·cm^{-1})	43	57	111	59	56
Temperature (°C)	16	15	16	15	16
Pe	4.9	4.2	3.8	4.6	4.9
Main elements					
HCO_3^- (mg·L^{-1})	12.2 (6)	22.1 (6)	61.0 (6)	26.9 (6)	17.2 (6)
Cl^- (mg·L^{-1})	3.3 (9)	4.9 (6)	2.7 (9)	2.7 (8)	2.6 (8)
SO_4^{2-} (mg·L^{-1})	5.4 (9)	3.4 (9)	3.0 (8)	3.5 (9)	4.6 (9)
Na^+ (mg·L^{-1})	6 1)	8 (2)	6 (1)	6 (2)	6 (1)
Ca^{2+} (mg·L^{-1})	3 (1)	4 (1)	13 (2)	6 (2)	5 (1)
Mg^{2+} (mg·L^{-1})	0.8 (5)	1.2 (6)	4.0 (10)	1.7 (7)	1.4 (6)
K^+ (mg·L^{-1})	1.0 (6)	1.6 (7)	2.1 (9)	1.5 (7)	1.4 (7)
Si (mg·L^{-1})	8 (1)	9 (2)	9 (1)	5 (6)	9 (1)
Fe (mg·L^{-1})	0.4 (1)	0.4 (1)	2.2 (1)	0.3 (4)	0.3 (1)
Isotopes					
^{208}Pb (µg·L^{-1})	< Q.L.	< Q.L.	< Q.L.	< Q.L.	0.8 (3)
^{238}U (µg·L^{-1})	0.7 (2)	2.9 (1)	< Q.L.	3.3 (1)	1.3 (1)
Trace elements					
As (µg·L^{-1})	5 (5)	13 (2)	< Q.L.	5(3)	5 (1)
Li (µg·L^{-1})	< Q.L.	< Q.L.	< Q.L.	< Q.L.	0.4 (2)
Mn (µg·L^{-1})	27 (12)	90(4)	8 (1)	39 (1)	9(1)
Sr (µg·L^{-1})	< Q.L.	30(2)	91 (5)	40 (6)	< Q.L.
Ti (µg·L^{-1})	1.5 (3)	< Q.L.	< Q.L.	< Q.L.	1.3 (3)
Zn (µg·L^{-1})	13 (4)	< Q.L.	< Q.L.	< Q.L.	9 (3)

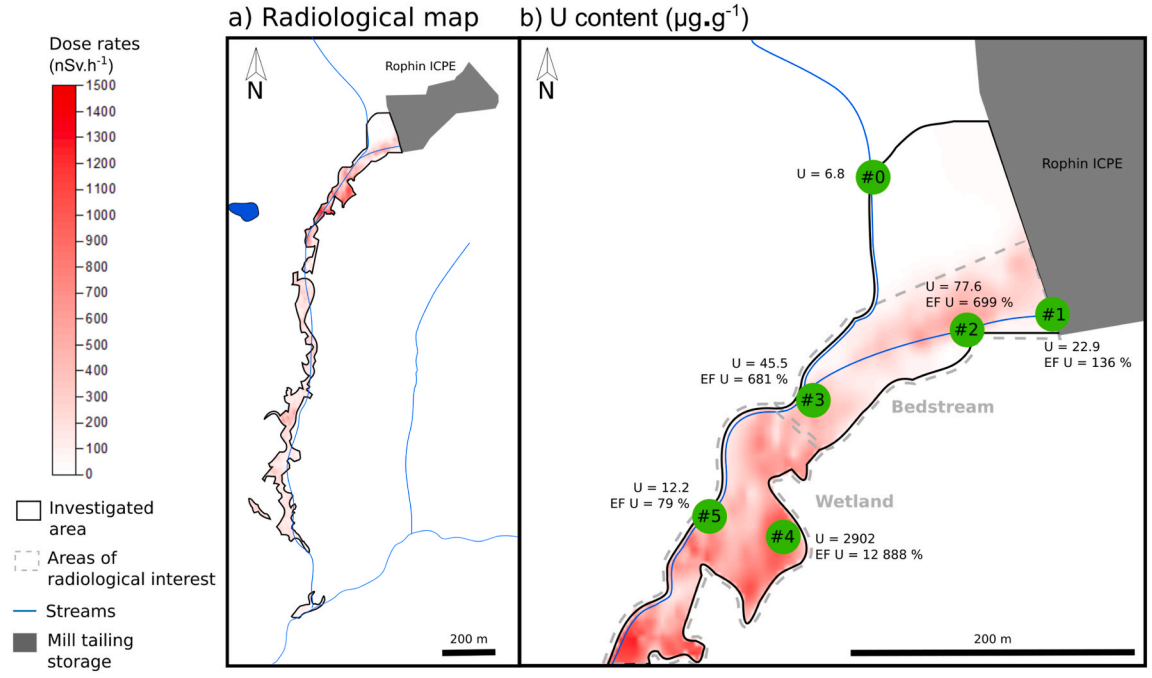

Fig. 2. (a): Radiological map of the area of study site. (b): focus on the study site and sampling points.

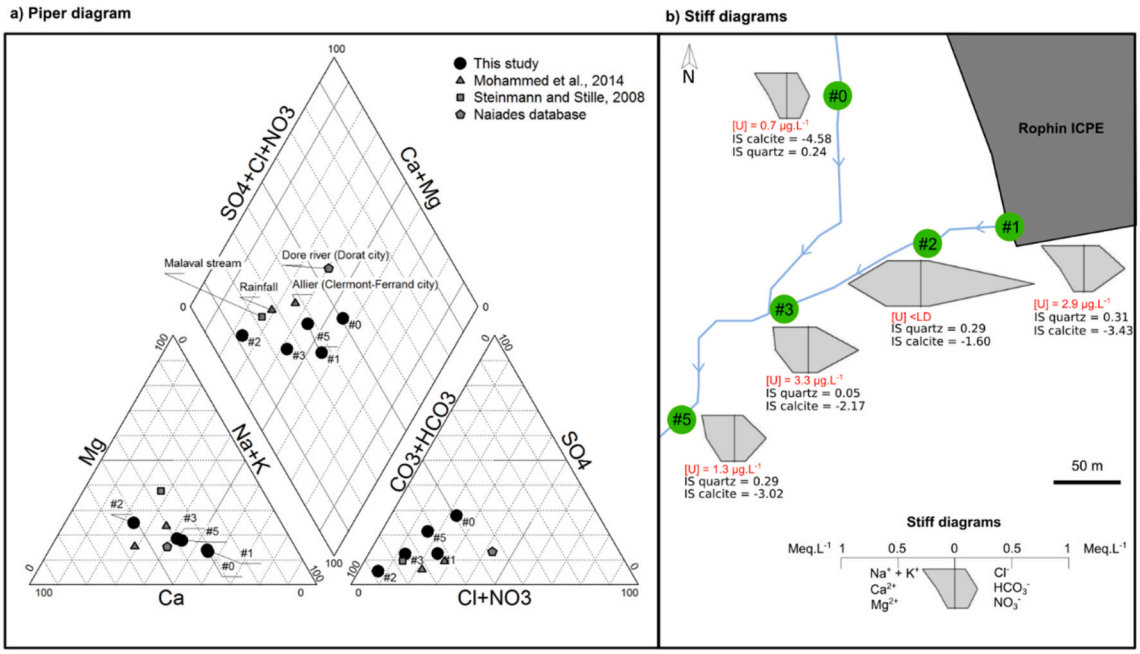

Fig. 3. (a): Plot of the stream water samples in a Piper diagram (filled circles: present data, filled triangles: rainwater, square: affluent of the Allier river in a granitic bedrock, stars: Allier and Dore rivers). (b): Stiff diagrams spatialized in the study area, with aqueous U concentration reported.

Ca^{2+} may originate from alteration of primary minerals (e.g. plagioclase) or from clay interlayer (see below). Finally, at point #2, aqueous ^{238}U concentration was below the detection limit, while Fe concentration was equal to 2.2(1) mg·L^{-1}, which suggests that the solution may have contained Fe colloids on which U may have been sorbed. For all other water samples, the ^{238}U concentrations (0.7–3.3 µg·L^{-1}) lie within the range of common surface waters (0.01–5 µg·L^{-1}, Ivanovich and Harmon, 1992), seawater (3.3 µg·L^{-1}) or the range of hydrothermal

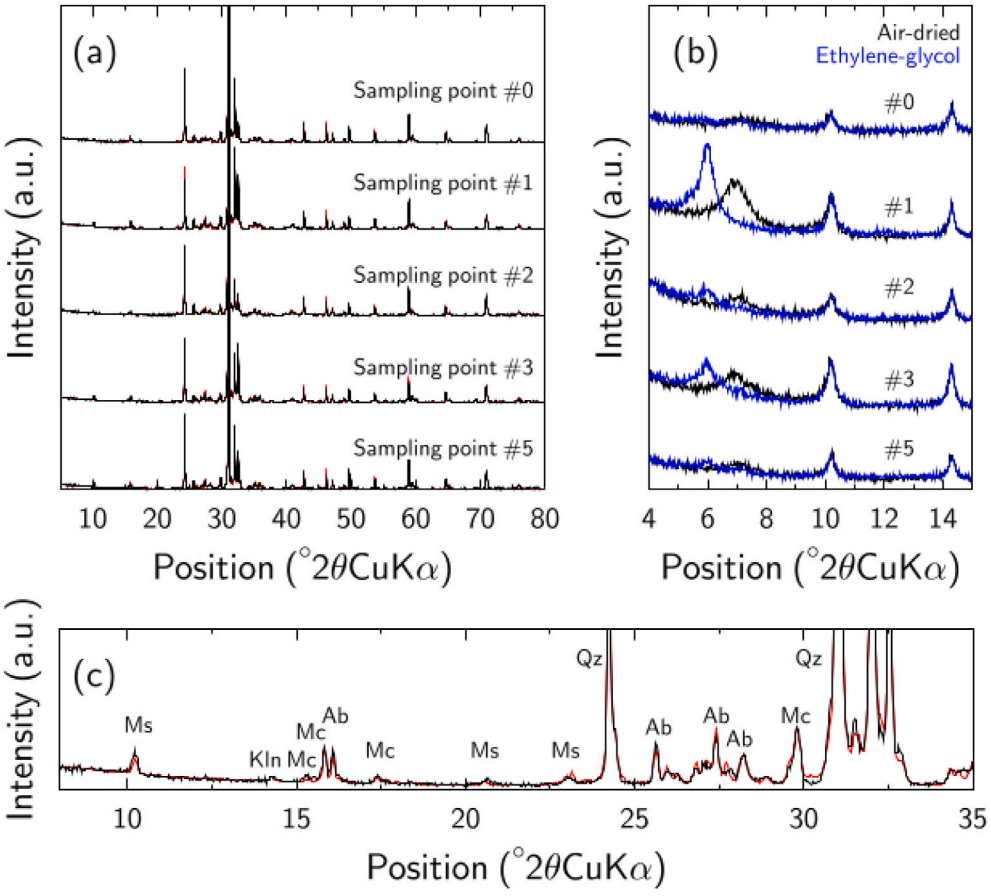

Fig. 4. (a): Experimental (black solid line) and modelled (red solid line) XRD patterns of, from top to bottom, sample #0, #1, #2, #3, and #5. (b): XRD patterns of oriented preparation in the air-dried (black solid line) and ethylene-glycol saturated (blue solid line) conditions. Patterns sorted as in the left panel. (c): detail of the XRD refinement from sampling point #1, to ease peak identification. Main diffraction are labelled according to: Ms = muscovite, Kln = kaolinite, Mc = microcline, Ab = albite, Qz = quartz.

springs from the same area (0.5–2 μg·L^{-1}, Rihs and Condomines, 2002). In all solution, Si was at equilibrium with quartz.

4.3. Mineralogy and chemistry of solid samples

4.3.1. Mineralogy of stream sediments

Sediment samples were dominantly coarse-grained with ~40% of >2 mm, ~30% of 0.5–2 mm, ~20% of 80–200 μm, and ~10% of <80 μm grains. They also had similar mineralogy (Fig. 4a, c and Table 3), with the main minerals being quartz (47.6–60 w%), feldspars (microcline – 21.5–23.5 w%), and plagioclase (albite – 11.6–23.1 w%). The samples also contained kaolinite (0.8–2.1 w%), muscovite (1–4.2 w%), and smectite (1.8–3.3 w%). Smectite was further studied by preparing oriented mounts on which, under air-dried conditions, a peak at about 7.1 °2θ CoKα (14 Å), faint in sample #0 and #5, was systematically observed (Fig. 4b). Upon saturation with ethylene-glycol (Fig. 4b), this peak shifted to about 5.9 °2θ CoKα (17 Å), which is a clue for smectite with interlayer Ca (Claret et al., 2004).

Further mineralogical identification, targeting phases that were too little abundant and (or) of too low crystallinity to be detected by XRD, was done with an optical microscope. The >500 μm grains were monocrystalline and polycrystalline elements of granite (K-feldspar, plagioclase, and muscovite), with minor biotite, Fe and Mn hydroxides, organic matter, and traces of phosphate minerals, monazite, and zircon. Biotite was often altered into chlorite and rutile. Plagioclase, and to a less extent K-feldspar grains had greyish aspect due to alteration. The low-altered grains had a fine sericite layer at their surface while the high altered were transformed into fine-grained clay minerals and Fe hydroxides. Plagioclase grains were partially weathered into kaolinite. Most coarse grains had a brownish coating of clay/Fe hydroxides. The <80 μm fraction was enriched in brownish clays, Fe and Mn (oxy)hydroxides, quartz and altered feldspars. Moreover, sediment samples #1 and #5 contained some elements of hydrothermal brecciated quartz with U ore, and Fe and Mn hydroxides. Collectively, these elements are representative of tectonic events and fluid circulations associated with deposition of primary U ore. SEM observations (Fig. 5) allowed identification of U-bearing phosphates: parsonite ($Pb_2(UO_2)(PO_4)_2{\cdot}2H_2O$) and autunite ($Ca(UO_2)_2(PO_4)_2{\cdot}10–12H_2O$), representative of U minerals of the Rophin primary ore. They were often but not systematically incorporated in a quartz matrix. Ce-monazites containing U and Pb were frequent <10-μm-sized grains included in granite minerals or in <63 μm fraction. Secondary jarosite-like phosphates, such as plumbogummite [$PbAl_3(PO_4)_2(OH)_6$], were also identified and contained variable As, Pb, Zn, Cu. Mn hydroxides contained K, U, Pb and Co, while Fe hydroxides did not contain U but As, Zn, and Co.

4.3.2. Total chemistry and enrichment factors

Sediment samples (Table 4) contained 77.3–77.8 w% SiO_2, 9.3–10.8 w% Al_2O_3, 3.8–5 w% K_2O, and 4.2–6.5 w% organic matter, exception made of sample #2 (10.6 w%). Such concentrations are, within 10% relative error, in agreement with XRD data: from the abundances of quartz (SiO_2), Microcline ($KAlSi_3O_8$), Albite ($NaAlSi_3O_8$, Smectite ($Ca_{0.3}Mg_{0.6}Al_{1.4}Si_4O_{10}(OH)_2$), Kaolinite ($Al_2Si_2O_5(OH)_4$), and Muscovite ($KAl_2(AlSi_3)O_{10}(OH)_2$), the samples would contain on average, according to XRD modeling, 85.9 wt% SiO_2, and 9.7 w% Al_2O_3, 4.3 wt% K_2O.

U concentration ranged from 6.8 to 77.6 μg·g^{-1}. MnO and Fe_2O_3 concentrations were respectively 0.01–0.29 w% and 0–3.5 w% and their maximum concentrations were not observed at the same sampling point: Fe_2O_3 was most abundant in sample #2, while MnO was most abundant in sample #3. TiO_2 concentration, which will be in the following used to calculate enrichment factors, was 0.06–0.10 w%. As, Ba, Li, Pb, Zn, and Sr were also quantified (Table 4) because they have contrasting geochemical properties, and their study is thus useful to the understanding of the geochemical cycles in the study area. Sediments of points #1, #2, #3, and #5 were enriched in As, Pb, and U as compared to those of sample #0 that are preserved from the direct influence of the ICPE.

Finally, the soil sample collected in the wetland was mainly composed of organic matter and SiO_2, each accounting for ~36 w% (Table 4). This sample also contained 11.3 w% Fe_2O_3, 7.7 w% Al_2O_3 and lower amounts of K_2O, TiO_2 and MnO (2.0 w%, 0.23 w% and 0.07 w%, respectively). This soil sample was enriched in many trace elements as compared to the sediment samples (Table 4). For example, U and Pb concentrations were 2902 and 1792 μg·g^{-1}, respectively.

Enrichment factors (EF; Table 5) allowed distinguishing several types of trace elements behavior. First, U EF in sediment samples from the stream downslope the ICPE increased from 136% at point #1 to 681–699% at points #2 and #3, and then decreased down to 79% at point #5. This could be interpreted as U mobilization by leaching or particulate transport of U-bearing phases from the tailing wastes, followed by either sedimentation between points #2 and #3 (e.g., due a decrease in the stream slope), precipitation of aqueous U due to changes in chemical conditions, or sorption of aqueous U by minerals such as Mn oxides (Rihs et al., 2005). Discrimination between these different hypotheses requires the analysis of topographic and sequential extraction data (see below). Sr EF was 2% at point #1. It then decreased down to −15% at point #2, increased to 54% at point #3, and finally decreased down to 12% at point #5. Li EF followed almost exactly the same trend (r^2 = 0.93). Since Li is enriched in clay minerals as compared to U-bearing minerals (Horstman, 1957; Levskii et al., 1970), and since Sr can occupy clay interlayer, the present association suggests that clays controlled the distribution of both Li and Sr. Arsenic EF reached 590% at point #2, coherent with the high As affinity for Fe oxides (Bataillard et al., 2014; Dixit and Hering, 2003) and the fact that point #2 is enriched in Fe oxides, as deduced both from field observations and from higher Fe content in point #2 as compared to points #1 and #3 (Table 4). However, because there is certainly particle sedimentation at point #2, and because U-bearing phosphate minerals that originate from the tailings contain As (Fig. 5b), the exact nature of As enrichment at point #2 cannot be elucidated by the sole study of EF. The highest EF of Ba, Pb, and Zn was observed at point #3, coherent with their high affinity for Mn oxides (Grangeon et al., 2012; Tonkin et al., 2004; Villalobos et al., 2005) and the fact that point #3 has the highest Mn content of all samples (Table 4). However, as for point #2, the likely particle deposition at point #3 makes that U-bearing phosphate minerals may play a role in observed Ba, Pb, and Zn EF, and in particular in Pb EF (Fig. 5). Finally, in the soil sample (#4), the large Pb (1013) and U (12 888) EF suggested a specific reactivity between these elements and organic matter.

Table 3
Quantitative mineralogy of studied samples.

Mineral	Abundance (w%) in sampling point				
	#0	#1	#2	#3	#5
Quartz	60.6(4)	47.6(4)	55.4(3)	51.7(4)	56.0(3)
Microcline	23.2(6)	21.6(7)	23.1(8)	23.5(8)	21.5(6)
Albite	11.6(5)	23.1(8)	13.0(4)	18.6(6)	17.4(7)
Smectite	2.5(4)	2.7(5)	3.3(4)	1.8(3)	1.8(4)
Kaolinite	1.1(2)	0.8(2)	2.1(2)	1.4(2)	0.8(2)
Muscovite	1.0(2)	4.2(2)	3.1(2)	3.0(2)	2.5(2)

4.3.3. Geochemical reservoirs of U and related elements in stream sediments

No significant amount of water-extractable elements was recovered at step 1 of the sequential extraction procedure (Table 6), as it could expected for a stream sediment, which is in perpetual contact with a continuously renewed solution of low ionic strength (Table 2). In contrast, and in agreement with XRD patterns suggesting that smectite interlayers contain predominantly Ca, 82–96% of total extractable Ca was recovered at step 2 (Table 6), which targets exchangeable ions in clay interlayer (Tessier et al., 1979) (see Table 1).

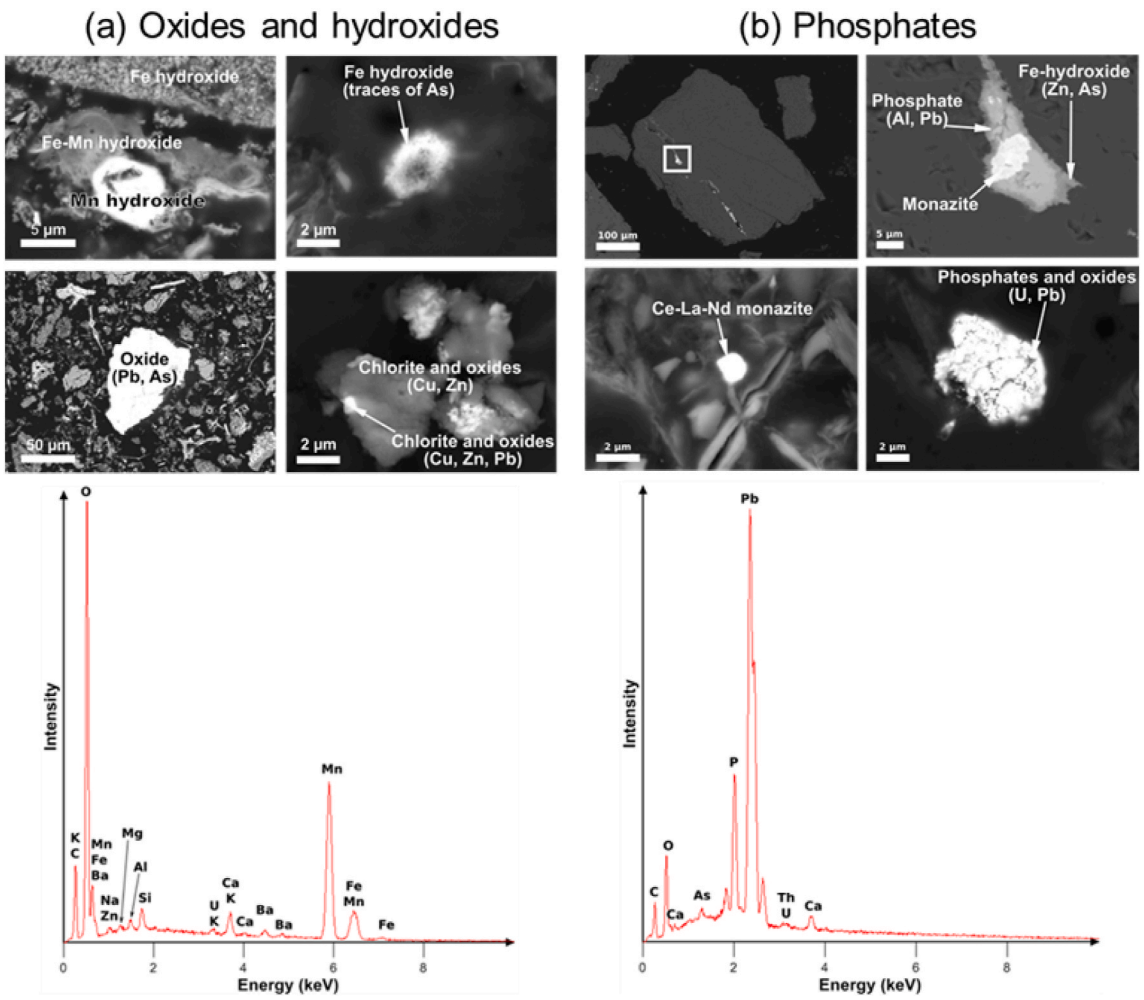

Fig. 5. SEM observations of (a) Fe and Mn oxides and (b) phosphate minerals, and associated EDX spectra (bottom of each panel, obtained from the grains shown in the top left panel in (a) and bottom right panel in (b)).

Table 4
Chemical composition of all studied samples.

Chemical element	Concentration					
	Point #0	Point #1	Point #2	Point #3	Point #4	Point #5
Major elements (w%)						
SiO_2	77.8	74.8	72.3	73.3	36.1	74.2
Al_2O_3	9.3	10.8	9.3	9.6	7.7	10.0
K_2O	4.8	5.0	3.8	4.4	2.0	5.0
Fe_2O_3	1	1.4	3.5	1.4	11.3	< QL
MnO	0.01	0.04	0.11	0.29	0.07	0.05
TiO_2	0.07	0.10	0.10	0.06	0.23	0.07
P_2O_5	0.07	0.09	0.10	0.09	0.30	0.08
CaO	< QL	< QL	< QL	< QL	< QL	< QL
Organic matter	6.5	4.2	10.6	5.7	36.0	5.6
Trace elements ($\mu g \cdot g^{-1}$)						
As	22	53	217	100	732	30
Ba	178	203	253	320	331	204
Li	10	21	18	17	27	13
Pb	49	365	254	416	1792	107
Sr	41	60	50	54	63	46
U	6.8	22.9	77.6	45.5	2902	12.2
Zn	16	26	37	46	100	25

Table 5
Enrichment factors of all trace elements of interest, at each sampling point but reference point #0.

Chemical element	Enrichment factor (%)				
	Point #1	Point #2	Point #3	Point #4	Point #5
As	69	590	430	913	36
Ba	−20	−1	110	−43	15
Li	47	26	98	−18	30
Pb	421	263	890	1013	118
Sr	2	−15	54	−53	12
U	136	699	681	12 888	79
Zn	14	62	235	90	56

At step 3, only P was preferentially released (36–100% of extractable PO_4), and this extraction step thus mainly affected phosphate minerals. As only ~1-2% of total PO_4 was extracted, this alteration was limited. While this was probably due to the fact that U-bearing phosphate minerals are often observed to be trapped in a quartz matrix (see above) and hence preserved from potential contact with any solution, it cannot be ruled out that this low extraction yield was also partially due to the presence of several ore phosphate minerals having different solubility.

33–68% of extractable Fe was leached during step 4, and this extraction step thus dissolved Fe oxides. Arbitrarily assuming that Fe was present at FeOOH, samples contained 0.04–0.11 w% Fe oxide (mean: 0.07 w%), coherent with the fact that they were not detected by XRD. At points #1, #3, and #5, Mn was also mainly extracted at step 4

Table 6
Summary of sequential extraction results. Not all major elements shown because some yields were negligible.

Chemical Element	Sampling point	Total concentration extracted		Amount extracted at a given extraction step (%)				
		($\mu g\ g^{-1}$)	% of total	Step 1	Step 2	Step 3	Step 4	Step 5
Major elements								
Fe	Point #0	724	11%	0	0	9	33	58
	Point #1	698	7%	0	0	26	65	8
	Point #2	1224	5%	0	0	12	57	30
	Point #3	584	6%	0	0	13	68	19
	Point #5	614	< Q.L.	0	0	16	63	21
Mn	Point #0	103	100%	3	71	13	5	8
	Point #1	420	100%	0	8	3	77	11
	Point #2	983	100%	2	67	17	9	5
	Point #3	3446	100%	1	8	6	82	4
	Point #5	481	100%	1	34	11	49	5
PO_4	Point #0	5.0	1%	0	0	78	22	0
	Point #1	20.7	2%	7	0	36	0	57
	Point #2	13.9	1%	0	0	100	0	0
	Point #3	13.3	1%	0	0	66	0	34
	Point #5	14.0	1%	16	0	54	8	22
Ca	Point #0	309	15%	0	96	4	0	0
	Point #1	259	9%	0	82	0	0	18
	Point #2	617	19%	2	85	8	0	4
	Point #3	578	29%	10	82	6	0	2
	Point #5	372	19%	3	94	3	0	0
Trace elements								
As	Point #0	2.5	11%	27	17	28	23	6
	Point #1	1.9	4%	22	15	48	12	3
	Point #2	2.6	1%	12	14	51	18	4
	Point #3	2.0	2%	8	14	70	3	4
	Point #5	1.7	6%	26	18	43	8	5
Ba	Point #0	20	11%	1	78	11	2	8
	Point #1	32	16%	0	37	5	41	18
	Point #2	61	24%	0	65	21	6	8
	Point #3	160	50%	0	26	20	46	8
	Point #5	35	17%	0	62	14	15	8
Li	Point #0	0.33	3%	6	5	7	10	72
	Point #1	0.70	3%	2	12	8	16	62
	Point #2	0.58	3%	6	15	7	9	63
	Point #3	0.25	1%	5	14	8	12	61
	Point #5	0.38	3%	3	14	10	9	64
Pb	Point #0	3.4	7%	0	5	59	0	36
	Point #1	88.0	24%	0	4	38	27	31
	Point #2	23.6	9%	0	3	92	1	5
	Point #3	87.5	21%	0	1	50	17	31
	Point #5	20.5	19%	0	3	59	5	33
Sr	Point #0	3.8	9%	3	85	5	1	7
	Point #1	4.9	8%	0	73	2	5	20
	Point #2	10.0	20%	2	78	10	3	7
	Point #3	10.6	20%	6	70	7	13	4
	Point #5	4.8	10%	3	84	4	2	7
U	Point #0	4.7	69%	1	9	48	0	43
	Point #1	13.9	61%	2	31	28	4	35
	Point #2	35.1	45%	0	6	58	0	36
	Point #3	31.3	69%	0	10	55	1	33
	Point #5	7.6	63%	2	13	52	0	33
Zn	Point #0	2.1	13%	0	6	31	16	46
	Point #1	2.2	8%	0	7	21	33	39
	Point #2	3.5	9%	0	7	36	23	33
	Point #3	17.9	39%	0	9	27	47	17
	Point #5	6.5	26%	0	17	33	26	24

(49–82% of total extractible Mn), which amounted to 0.001–0.44 w% MnO_2 (mean: 0.11 w%). Associated with the fact that point #3 had the highest Mn content (0.29 w% MnO), it was concluded that step 4 also dissolved Mn oxides. Mn was also significantly recovered at step 2 (8–71% of total extractible Mn), suggesting either that clay interlayer also contained Mn or that the acidic pH at step 2 induced a limited dissolution of Mn oxides. However, even if all Mn extracted at step 2 originated from clay interlayer, the cationic composition of the clay interlayer would remain largely dominated by Ca, as the Ca/Mn recovered at step 2 was on average 4 $mol{\cdot}mol^{-1}$. At point #3, the Fe/Mn ratio extracted at step 4 was 0.14 $mol{\cdot}mol^{-1}$, and hence this sample contained more Mn oxides than Fe oxides. For all other sampling points, Fe/Mn was higher than 1, suggesting that they contained more Fe oxides than Mn oxides, with a Fe/Mn increasing in the order point #1 (1.4 $mol{\cdot}mol^{-1}$), #5 (1.6 $mol{\cdot}mol^{-1}$), #2 (7.8 $mol{\cdot}mol^{-1}$), and #0 (45.6 $mol{\cdot}mol^{-1}$). Finally, step #5, targeting organic matter, did mainly release in solution Fe and PO_4, two constituents of natural organic matter (Rose and Waite, 2003; Stewart and Cole, 1989).

To summarize, it is proposed that steps 1, 2, 3, 4, and 5 released in solution elements that were sorbed or incorporated in, 1) water-soluble phases, 2) clays, 3) phosphate minerals, 4) Fe and Mn oxides, and 5) organic matter. Note that Mn extraction yields were rounded to 100% because the low content in the bulk sediment (Table 4) limited the accuracy of quantification of total Mn in the solid and because, within

analytical uncertainties, those yields were 100%.

In sample #0, collected in the stream not directly under influence of the ICPE, 4.7 $\mu g \cdot g^{-1}$ U was extractable (69% of total U). It was mainly associated to phosphate minerals (48% of total extractable U) and to organic matter (43% of total extractable U). A minor amount (9%) was associated to clays, and most likely located in clay interlayer as a result of acidic and low ionic strength stream waters (Table 2, Tournassat et al., 2018). Because the stream circulating at point #0 was not connected to the ICPE, the phosphate minerals were either transported from the wastes by eolian transport, naturally present, or originated from an another site containing phosphate minerals (e.g., the Gagnol site). U associated to smectite and organic matter was probably adsorbed *in situ* following U leaching from primary phases. In this stream sample, as well as in other stream samples, U that could not be extracted certainly corresponded to the U-bearing phosphate minerals included in a quartz matrix and hence not accessible to the solution. Downstream from the ICPE (sample #1), total extractable U concentration was 13.9 $\mu g \cdot g^{-1}$ (61% of total U), about three times higher than in sample #0, with the clay, phosphate and organic matter reservoirs accounting each for about 1/3 of total extractable U. A minor fraction of extractable U (4%) was associated to Fe/Mn oxides. Downstream, in sample #2, total extractable U concentration increased to 35.1 $\mu g \cdot g^{-1}$ (45% of total U), and the two main reservoirs were phosphates (58% of total extractable U) and organic matter (36% of total extractable U). At point #3, at the confluence of streams flowing through point #0 or point #1, total extractable U concentration was 31.3 $\mu g \cdot g^{-1}$ (69% of total U), similar to point #2, and the solid phase speciation was within uncertainties similar to that of point #2, except for a possible minor contribution of Fe/Mn oxides (1% of extractable U). Similarly, at point #5, downstream point #3, total U concentration decreased to 7.6 $\mu g \cdot g^{-1}$ (63% of total U), but the relative proportions associated to all chemical reservoirs remained similar. Since the soil sample (point #4) had high organic matter content (36 w%), it could not be investigated by the presently used sequential extraction procedure, but the high U enrichment factor suggested that U was mainly bounded to organic matter. A statistical analysis confirmed that U was statistically associated to PO_4 in stream sediments and hence to phosphate minerals (Fig. 6), as As and Pb were, coherent with SEM observations (Fig. 5).

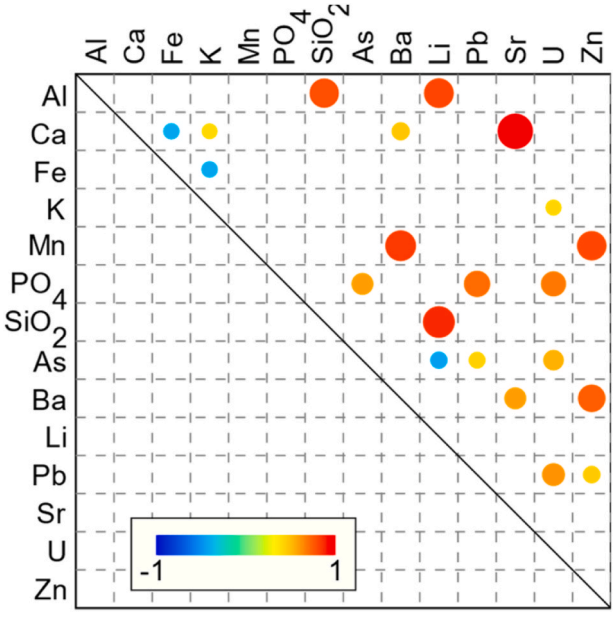

Fig. 6. Pearson's correlation coefficient for every pairs of elements analyzed in this study, calculated from amounts extracted during the sequential extraction procedure. Only statistically robust (*p-value* > 0.05) values reported. Autocorrelations not shown. Correlation coefficient increases from −1 to 1 with colour, in the order blue, cyan, green (correlation coefficient = 0), yellow, orange, red, and with symbol size.

In contrast to U, adsorption processes significantly affected Zn solid speciation along the stream profile: the highest Zn concentration was observed at point #3, where Mn oxides were abundant (Table 4), coherent with Zn affinity for Mn oxides (Grangeon et al., 2012) and with Zn–Mn correlation (Fig. 6). Ba had apparently an even more complex behavior, with the distribution between the different reservoirs depending on the sample, but the correlation analysis showed that its distribution was also controlled by Mn oxides (Fig. 6). Finally, the Li–Si correlation (Fig. 6) is coherent with the reservoir of these elements being clay minerals, and is supported by the fact that Li is mainly recovered at step 5, which is the sole step inducing significant (up to 20%) dissolution of smectite layer (as exemplified with saponite and nontronite - Ryan et al., 2008). With a Li content in smectite of about 50 $\mu g \cdot g^{-1}$ (Horstman, 1957) and a Li content recovered at step 5 of 0.15–0.43 $\mu g \cdot g^{-1}$ (Table 6), the deduced smectite content in the samples is 2–4 w% (average: 2.9%), in agreement with Rietveld quantification of XRD data (Table 3).

4.4. *Relative roles of geochemical processes and particulate transport on U migration in the streams*

The distribution of U in the studied area was the result of the interplay between partial dissolution of primary ore minerals, transport of dissolved U in the stream, adsorption processes, and particulate transport of primary ore phosphate minerals. The relative influence of these phenomena at a given point depended on the distance to the source (Rophin ICPE) and on the slope of the streambed. In the ore, U was associated to phosphate minerals. With time, weathering of the tailings certainly led to the formation of aqueous U that was then adsorbed by the most reactive phases, namely organic matter, clay minerals, and, when present, Fe/Mn oxides. In sample #1, which is the closest to the ICPE output and which is characterized by a steep streambed slope, total U concentration was 22.9 $\mu g \cdot g^{-1}$, of which 61% was extracted by present sequential extraction procedure. Extractable U was about evenly distributed in phosphates, clays, and organic matter. A minor fraction (4% of extractible U) was associated to Fe/Mn oxides. Since non-extractable U (in ore minerals included in a quartz matrix – see discussion above and Fig. 5) plus U extracted at step 3 of the sequential extraction procedure represented 56% of total U, it can be concluded that, at point #1, the main factor affecting U distribution was particulate transport. Geochemical sorption reactions however played a significant role, with aqueous U being sorbed by clays, organic matter, and to a lesser extent Fe/Mn oxides. At point #2, the streambed slope reduced significantly, U concentration in the solid increased to 77.6 $\mu g \cdot g^{-1}$, and ore minerals were by far the main U reservoir (55% of total U in the residual fraction plus 58% of the 35.1 $\mu g \cdot g^{-1}$ extractible U). Organic matter and clays accounted respectively for 6% and 36% of extractible U. The most likely explanation was particle deposition at point #2 favoured by the decrease in streambed slope that would have induced preferential deposition of U-bearing phases, namely extractible and non-extractible U ore minerals. This hypothesis was supported by the fact that As, whose main bearing phase was phosphate minerals (Figs. 5 and 6), had a higher concentration at point #2 than at point #1 (Table 1), had a higher enrichment factor (Table 5), and was mainly extracted at step 3 of the sequential extraction procedure (Table 6). At point #3, the concentration of extractible U associated to organic matter, clays, and phosphates was close to that of point #2, suggesting that the related minerals were equally transported in the stream, without preferential deposition between points #2 and #3. In contrast, non-extractible U-bearing phases (certainly ore minerals within a quartz matrix and hence of bigger size than extractible phosphate minerals) were preferentially deposited at point #2, since the total U concentration decreased from point #2 to point #3. Also, at point #3, 1% of extractible U was associated to Fe/Mn oxides. Since Mn has its highest extraction yield at point #3, and since U has high affinity for Mn oxides, it can be speculated that,

at point #3, Mn oxides played a minor yet quantifiable role in U speciation, through adsorption of aqueous U. Such data interpretation was supported by several observations. First, not all samples had U recovered at step 4 of the sequential extraction procedure. Because all samples had similar mineralogy (Table 3), a leaching or partial dissolution of a mineral that would not have been Fe/Mn oxides and that would not have occurred in all samples is unlikely and hence it is assumed that step 4 only extracted Fe/Mn oxides. Second, U was only recovered at step 4 for the samples collected at point #1 and #3, which are the two samples that had the highest Mn extraction yield at step 4 of the sequential extraction procedure, while Fe did not exhibit such specific behaviour. Third, the U/Mn ratios calculated from the amounts extracted at step 4 were 4 10^{-4} (point #1) and 2 10^{-5} mol·mol^{-1}. Such values in good agreement with values expected for adsorption equilibrium with birnessite (6.6 10^{-5} to 4.8 10^{-4} mol·mol^{-1} when aqueous U concentration is in the µmol range - Rihs et al., 2005), the probably most common Mn oxide in the environment (Grangeon et al., 2020). Finally, at point #5, the relative proportions of U associated to organic matter, clays and extractible phosphate minerals were similar to that observed at points #2 and #3, but the concentration was significantly reduced, from 31.3-35.1 µg·g^{-1} to 7.6 µg·g^{-1}. The proportion of extractible to total U was 62%, close to that of point #3 (69%). Such behaviour was most likely explain by a mixing with U-free sediments of the Gourjeat stream.

To summarize (Fig. 7), at point #1, which is the closest to the ICPE and where streambed slope is steep, the main mechanism of U retention was deposition of phosphate minerals, but adsorption of aqueous U by organic matter, clays, and Fe/Mn oxides played an almost equal role. This led to a U concentration in the sediment of 22.9 µg·g^{-1}. At point #2, characterized by a decrease in streambed slope, preferential deposition of ore minerals was the main factor controlling sediment U concentration, while sorption by U-bearing organic matter and clays had a minor influence. Further away, at points #3 and #5, the particle sedimentation processes were almost similar. The sole difference resided in the fact that, at point #3, Mn oxides play a minor role in adsorbing aqueous U and that, at point #5, there was mixing of the U-containing sediments with the U-free sediments from a second stream.

4.5. U and other elements distribution between fresh and developed soil organic matter of the wetland

U concentration at point #4 (2902 µg·g^{-1}, see Table 4) was in agreement with values reported by Martin and coworkers (Martin et al., 2020, 2021) and is, to our knowledge, the highest reported in the literature for such a site. Cuvier et al. (2015) measured concentrations in the same order of magnitude, yet about two times lower, downstream another French former U mine (Bertholène, France). It is also important to note that, according to the MIMAUSA database distributed by IRSN, all samples were collected in the Rophin mine footprint. Given that organic matter was the main soil component at this sampling point (Table 4) and that overall U distribution is controlled by this phase (Martin et al., 2020, 2021), we focused in this section on the association with organic matter.

A selective extraction procedure was performed to quantify the distribution of U and other elements between two types of organic matter: humic and fulvic acids, representative of the humified soil organic matter, and other components of higher molecular weight (e.g., lignin, termed here "fresh organic matter"). Of all major elements, only Fe and Mn were significantly extracted by this procedure (15% of total Mn and 23% of total Fe - Table 7). Mn was about evenly distributed between fresh and humified organic matter, with relative fractions of 59% and 41%, respectively (Table 7). Such association between organic matter and Mn, and the even distribution between the two reservoirs, is consistent with our knowledge of Mn cycling in the litter (Keiluweit et al., 2015), with Mn^{2+} being present in fresh organic matter and then being at least partly transformed to Mn^{3+} by fungi during organic matter degradation. As Mn^{3+}, it plays an active role in litter degradation and is finally incorporated in humified organic matter as Mn^{3+} or reduced Mn^{2+}. $Mn^{2+/3+}$ remains in humified organic matter for a few years before transforming to $Mn^{3+/4+}$ oxides (here, the fraction that was not extracted). In contrast to Mn, 97% of extractable Fe was associated to humified organic matter, coherent with previous observations (Hiraide et al., 1988).

The main U-bearing phase in sample #4 was organic matter (63% of total U - Table 7). Of this fraction associated to organic matter, 48% was

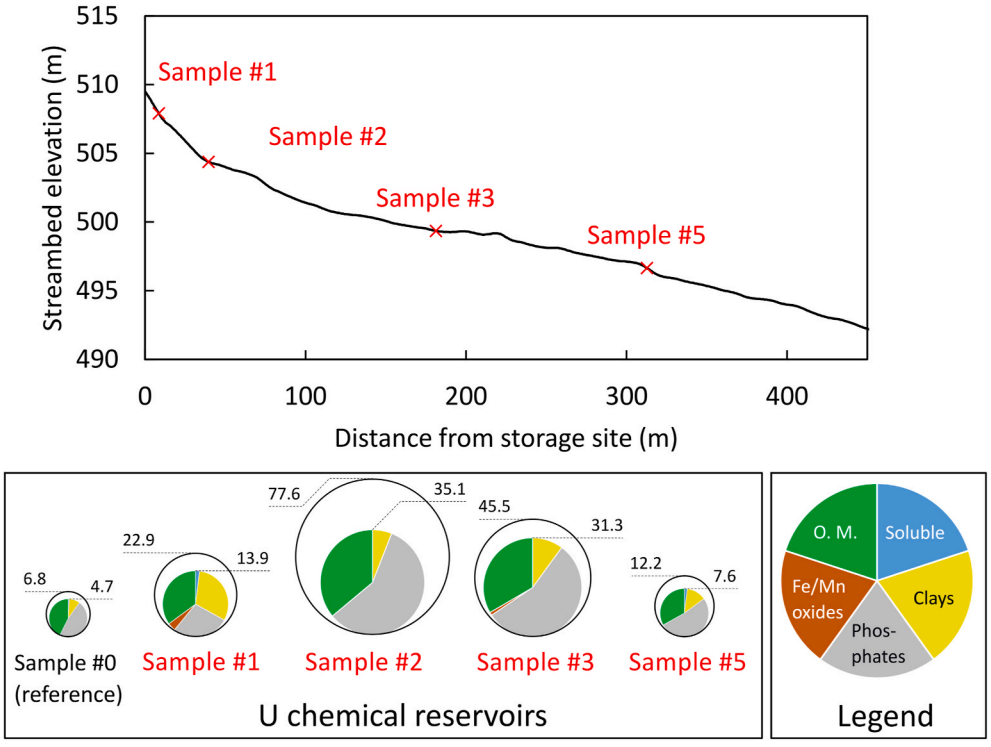

Fig. 7. Topographic profile of the stream passing at point #1 (top) and summary of main U chemical reservoirs in the streams, at each sampling point (bottom left). All circle areas are proportional to U concentration at a given point. Open black circles: total U concentration. Pie charts: U speciation, as determined by the sequential extraction scheme. Blue, yellow, grey, brown, and green materialize the proportion of extractible U associated to, respectively, water soluble phases, clay interlayers, extractible phosphate minerals, Fe/Mn oxides, and organic matter (see legend at the bottom right of the figure).

Table 7
Amount of elements, expressed as absolute (μg·g^{-1}) and relative (% of total abundance in the sample – Table 4) values, extracted during the two steps of selective extraction targeting organic matter ("O.M.").

Chemical element	Concentration extracted		% associated to humified O.M.	% associated to fresh O.M.
	μg·g^{-1}	% of total		
Major elements				
SiO_2	3713 (554)	1	86	14
Al_2O_3	3533 (144)	5	63	37
K_2O	419(17)	2	57	43
Fe_2O_3	25 538 (1512)	23	97	3
MnO	107(10)	15	41	59
PO_4	< Q.L.	< Q.L.	< Q.L.	< Q.L.
Ca	350(18)	< Q.L.	54.0	46.0
Trace elements				
As	62(2)	8	100	0
Ba	43(2)	13	42	58
Li	0.19(3)	1	84	16
Pb	315(13)	18	99	1
Sr	3.1(1)	5	39	61
U	1830(59)	63	52	48
Zn	4(1)	4	58	42

associated to fresh organic matter. The other U-bearing phases, which have minor contribution, are Mn/Fe oxides and U-bearing ore minerals (Martin et al., 2021). This suggests that the mechanism of U incorporation in the soil is not only sorption on humified organic matter, but also and at least partly uptake by the living.

The association of U with fresh organic matter was consistent with the fact that, in the presently studied wetland, the trunks of oaks contain higher U concentrations compared to the geochemical background (Martin et al., 2020). Thus, trees certainly uptake U, a mechanism that occurs preferentially at pH values < 5.5 (Ebbs et al., 1998) that are found in soils rich in organic matter, as the present one. U was probably translocated in the foliage before leaves fall and accumulation in the first centimeters of the soil that was sampled here. Such translocation has for example been observed in deciduous (Acer pseudoplatanus, Quercus sp.) and evergreen (Picea abies, Pinus silvestris) trees grown on U-containing mine tailings (Märten et al., 2015, 2015t; Štrok et al., 2011). U association to humified organic matter is explained by its sorption by humic acids during the humification process that occurs after the fall of leaves (Szalay, 1964). This is supported by the fact that in the studied wetland, U concentration increased with depth (i.e. with increasing degree of humification) until a mineral horizon is reached (Martin et al., 2020).

For all other trace elements, less than 15% of the total concentration was associated with organic matter, exception made of Pb for which 18% of total extractible content was associated to organic matter and almost exclusively (99% of Pb associated to organic matter) to humified organic matter (Table 7). Pb has high affinity for humid and fulvic acids, even higher than for iron oxides at acidic pH values found in organic-rich horizons (Gustafsson et al., 2011), and Pb is thus certainly incorporated in the soil by sorption on humified organic matter.

5. Summary and conclusions

This study aimed at characterizing U and associated elements downslope Rophin ICPE, a former U mine, including the radiological context. Three different radiological zones of interest were defined: the geological background (below 200 nSv.h^{-1}), a streambed downstream the ICPE (between 200 and 800 nSv.h^{-1}) and a radiologically marked wetland (up to 1000 nSv.h^{-1}). Stream water samples had low U concentration, but the sediments contained up to 77.6 μg·g^{-1} U. The wetland soil contained 2902 μg·g^{-1} U.

It was concluded here that U was distributed between primary ore minerals (phosphates), clays, and organic matter, with phosphate minerals being certainly the main contributor to U particulate transport in the streambed, and clay and organic matter being secondary associations. U association to fresh organic matter in the wetland soil sample was a clue for probable U uptake by the living. Such hypothesis however deserves future investigations that would also be needed to get more insights on the complex and dynamic geochemical and particulate transport system.

Author statement

Romain Beuzeval: Investigation **Patrick Chardon:** Investigation, Writing – Review & Editing, Validation **Francis Claret:** Review & Editing, Project administration **Sylvain Grangeon:** Methodology, Validation, Formal analysis, Conceptualization, Visualization, Writing – Review & Editing **Thomas Grangeon**: Validation, Writing - Review & Editing, Project administration, Funding acquisition **Catherine Lerouge**: Investigation, Writing – Review & Editing **Gilles Montavon:** Conceptualization, Validation, Writing – Review & Editing, Supervision, Project administration, Funding acquisition **Celine Roux**: Investigation, Writing-Original Draft, Visualization, Formal analysis.

Data availability

Data will be made available on request.

Acknowledgments

The authors would like to thank the Carnot Institutes Network (inter-Carnot NNPHY 50314 "GSMU") and POLLUSOLS projects for funding this study. They also would like to thank the ZATU network and Lachaux city office. Julie Champion, Christophe Den Auwer, Hervé Michel, and Gabriel Manie, are acknowledged for their help in the sampling campaign and Catherine Landesman for her help on preliminary field investigations. The SMART team (Subatech) is thanked for his for technical support in radiological investigations, and particularly Mickael Bailly and Elodie Cormier for gamma analyses of samples and their helps on gamma ray peak interpretations. Cedric Duee (BRGM) is thanked for the SEM observations, Nicolas Maubec (BRGM) for X-Ray diffraction analyses, Veronique Baty (Subatech) for major chemicals analyses of water samples, and Mathieu Debure (BRGM) for technical support at the beginning of the investigation. S.G., T.G, and F.C. acknowledge funding by an internal research project (TransPORE). All authors thank Dr C S Eckley (associate editor) for his editorial handling and two anonymous reviewers for their detailed and very constructive reviews, which helped improving significantly the quality of the present manuscript.

References

Ballouard, C., Poujol, M., Zeh, A., 2018. Multiple crust reworking in the French Armorican Variscan belt: implication for the genesis of uranium-fertile leucogranites. Int. J. Earth Sci. 107 (7), 2317–2336.

Barescut, J.C., Gariel, J.C., Péres, J.M., Servant, A.C., Herbelet, J., Daroussin, J.L., 2005. State of the environment around uranium mining sites (MIMAUSA: memory and Impact of (French) Mining sites for urAniUm: synthesis and Archives). Radioprotection 40 (S1), S803–S809.

Bataillard, P., Grangeon, S., Quinn, P., Mosselmans, F., Lahfid, A., Wille, G., Joulian, C., Battaglia-Brunet, F., 2014. Iron and arsenic speciation in marine sediments undergoing a resuspension event: the impact of biotic activity. J. Soils Sediments 14 (3), 615–629.

Bermudez, G.M.A., Moreno, M., Invernizzi, R., Plá, R., Pignata, M.L., 2010. Evaluating top soil trace element pollution in the vicinity of a cement plant and a former open-cast uranium mine in central Argentina. J. Soils Sediments 10 (7), 1308–1323.

Bister, S., Birkhan, J., Lüllau, T., Bunka, M., Solle, A., Stieghorst, C., Riebe, B., Michel, R., Walther, C., 2015. Impact of former uranium mining activities on the floodplains of the Mulde River, Saxony, Germany. J. Environ. Radioact. 144, 21–31.

Boekhout, F., Gérard, M., Kanzari, A., Michel, A., Déjeant, A., Galoisy, L., Calas, G., Descostes, M., 2015. Uranium migration and retention during weathering of a granitic waste rock pile. Appl. Geochem. 58, 123–135.
Bouchot, V., Ledru, P., Lerouge, C., Lescuyer, J.-L., Milesi, J.-P., 2005. 5: late Variscan mineralizing systems related to orogenic processes: the French Massif Central. Ore Geol. Rev. 27 (1), 169–197.
Bresson, C., Ansoborlo, E., Vidaud, C., 2011. Radionuclide speciation: a key point in the field of nuclear toxicology studies. J. Anal. At. Spectrom. 26 (3), 593–601.
Breward, N., Peachey, D., 1983. The development of a rapid scheme for the elucidation of the chemical speciation of elements in sediments. Sci. Total Environ. 29 (1), 155–162.
Bril, H., Marignac, C., Cathelineau, M., Tollon, F., Cuney, M., Boiron, M.C., 1994. Metallogenesis of the French massif central: time-space relationships between ore deposition and tectono-magmatic events. In: Chantraine, J., Rolet, J., Santallier, D. S., Piqué, A., Keppie, J.D. (Eds.), Pre-Mesozoic Geology in France and Related Areas. Springer Berlin Heidelberg, Berlin, Heidelberg, pp. 379–402.
Claret, F., Lerouge, C., Laurioux, T., Bizi, M., Conte, T., Ghestem, J.P., Wille, G., Sato, T., Gaucher, E.C., Giffaut, E., Tournassat, C., 2010. Natural iodine in a clay formation: implications for iodine fate in geological disposals. Geochem. Cosmochim. Acta 74 (1), 16–29.
Claret, F., Sakharov, B.A., Drits, V.A., Velde, B., Meunier, A., Griffault, L., Lanson, B., 2004. Clay minerals in the Meuse-Haute Marne underground laboratory (France): possible influence of organic matter on clay mineral evolution. Clay Clay Miner. 52 (5), 515–532.
Cuvier, A., Panza, F., Pourcelot, L., Foissard, B., Cagnat, X., Prunier, J., van Beek, P., Souhaut, M., Le Roux, G., 2015. Uranium decay daughters from isolated mines: accumulation and sources. J. Environ. Radioact. 149, 110–120.
Di Giulio, R.T., Ryan, E.A., 1987. Mercury in soils, sediments, and clams from a North Carolina peatland. Water Air Soil Pollut. 33 (1), 205–219.
Dixit, S., Hering, J.G., 2003. Comparison of arsenic(V) and arsenic(III) sorption onto iron oxide minerals: implications for arsenic mobility. Environ. Sci. Technol. 37 (18), 4182–4189.
Doebelin, N., Kleeberg, R., 2015. Profex: a graphical user interface for the Rietveld refinement program BGMN. J. Appl. Crystallogr. 48 (5), 1573–1580.
Ebbs, S.D., Brady, D.J., Kochian, L.V., 1998. Role of uranium speciation in the uptake and translocation of uranium by plants. J. Exp. Bot. 49 (324), 1183–1190.
Gatehouse, S., Russell, D.W., Van Moort, J.C., 1977. Sequential soil analysis in exploration geochemistry. In: Butt, C.R.M., Wilding, I.G.P. (Eds.), Developments in Economic Geology. Elsevier, pp. 483–494.
Grangeon, S., Bataillard, P., Coussy, S., 2020. The nature of manganese oxides in soils and their role as scavengers of trace elements: implication for soil remediation. In: van Hullebusch, E.D., Huguenot, D., Pechaud, Y., Simonnot, M.-O., Colombano, S. (Eds.), Environmental Soil Remediation and Rehabilitation: Existing and Innovative Solutions. Springer International Publishing, Cham, pp. 399–429.
Grangeon, S., Manceau, A., Guilhermet, J., Gaillot, A.-C., Lanson, M., Lanson, B., 2012. Zn sorption modifies dynamically the layer and interlayer structure of vernadite. Geochem. Cosmochim. Acta 85, 302–313.
Grangeon, S., Vinsot, A., Tournassat, C., Lerouge, C., Giffaut, E., Heck, S., Groschopf, N., Denecke, M.A., Wechner, S., Schäfer, T., 2015. The influence of natural trace element distribution on the mobility of radionuclides. The exemple of nickel in a clay-rock. Appl. Geochem. 52, 155–173.
Guédron, S., Grangeon, S., Jouravel, G., Charlet, L., Sarret, G., 2013. Atmospheric mercury incorporation in soils of an area impacted by a chlor-alkali plant (Grenoble, France): contribution of canopy uptake. Sci. Total Environ. 445–446, 356–364.
Guedron, S., Grangeon, S., Lanson, B., Grimaldi, M., 2009. Mercury speciation in a tropical soil association; Consequence of gold mining on Hg distribution in French Guiana. Geoderma 153 (3), 331–346.
Guedron, S., Grimaldi, C., Chauvel, C., Spadini, L., Grimaldi, M., 2006. Weathering versus atmospheric contributions to mercury concentrations in French Guiana soils. Appl. Geochem. 21 (11), 2010–2022.
Gustafsson, J.P., Tiberg, C., Edkymish, A., Kleja, D.B., 2011. Modelling lead(II) sorption to ferrihydrite and soil organic matter. Environ. Chem. 8 (5), 485–492.
Hammer, Ø., Harper, D.A., Ryan, P.D., 2001. PAST: paleontological statistics software package for education and data analysis. Palaeontol. Electron. 4 (1), 9.
Himeur, N., 2010. Bilan Environemental. Sites miniers du Puy-de-Dôme. AREVA.
Hiraide, M., Ishii, M., Mizuike, A., 1988. Speciation of iron in river water. Anal. Sci. 4 (6), 605–609.
Horstman, E.L., 1957. The distribution of lithium, rubidium and caesium in igneous and sedimentary rocks. Geochem. Cosmochim. Acta 12 (1), 1–28.
Ivanovich, M., Harmon, R.S., 1992. Uranium-series Disequilibrium: Applications to Earth, Marine, and Environmental Sciences.
Keiluweit, M., Nico, P., Harmon, M.E., Mao, J., Pett-Ridge, J., Kleber, M., 2015. Long-term litter decomposition controlled by manganese redox cycling. Proc. Natl. Acad. Sci. USA 112 (38), E5253–E5260.
Levskii, L.K., Murin, A.N., Zaslavskii, V.G., 1970. Isotopic abundance of lithium in uranium minerals. Sov. Atom. Energy 28 (4), 443–445.
Lind, O.C., Stegnar, P., Tolongutov, B., Rosseland, B.O., Strømman, G., Uralbekov, B., Usubalieva, A., Solomatina, A., Gwynn, J.P., Lespukh, E., Salbu, B., 2013. Environmental impact assessment of radionuclide and metal contamination at the former U site at Kadji Sai, Kyrgyzstan. J. Environ. Radioact. 123, 37–49.
Lottermoser, B.G., Ashley, P.M., 2005. Tailings dam seepage at the rehabilitated Mary Kathleen uranium mine, Australia. J. Geochem. Explor. 85 (3), 119–137.
Marignac, C., Cuney, M., 1999. Ore deposits of the French Massif Central: insight into the metallogenesis of the Variscan collision belt. Miner. Deposita 34 (5), 472–504.
Märten, A., Berger, D., Köhler, M., Merten, D., 2015. The dendroanalysis of oak trees as a method of biomonitoring past and recent contamination in an area influenced by uranium mining. Environ. Sci. Pollut. Res. 22 (24), 19417–19425.
Martin, A., Hassan-Loni, Y., Fichtner, A., Péron, O., David, K., Chardon, P., Larrue, S., Gourgiotis, A., Sachs, S., Arnold, T., Grambow, B., Stumpf, T., Montavon, G., 2020. An integrated approach combining soil profile, records and tree ring analysis to identify the origin of environmental contamination in a former uranium mine (Rophin, France). Sci. Total Environ. 747, 141295.
Martin, A., Montavon, G., Landesman, C., 2021. A combined DGT - DET approach for an in situ investigation of uranium resupply from large soil profiles in a wetland impacted by former mining activities. Chemosphere 279, 130526.
Meyer-Georg, S., 2021. Study of the Speciation and Mobility of Uranium (VI) in Natural Waters : Effect of Organic Matter. Université de Strasbourg.
Minouflet, M., Ayrault, S., Badot, P.-M., Cotelle, S., Ferard, J.-F., 2005. Assessment of the genotoxicity of 137Cs radiation using Vicia-micronucleus, Tradescantia-micronucleus and Tradescantia-stamen-hair mutation bioassays. J. Environ. Radioact. 81 (2), 143–153.
Mohammed, N., Celle-Jeanton, H., Huneau, F., Le Coustumer, P., Lavastre, V., Bertrand, G., Charrier, G., Clauzet, M.L., 2014. Isotopic and geochemical identification of main groundwater supply sources to an alluvial aquifer, the Allier River valley (France). J. Hydrol. 508, 181–196.
Møller, A.P., Mousseau, T.A., 2011. Conservation consequences of Chernobyl and other nuclear accidents. Biol. Conserv. 144 (12), 2787–2798.
Neiva, A.M.R., Carvalho, P.C.S., Antunes, I.M.H.R., Silva, M.M.V.G., Santos, A.C.T., Cabral Pinto, M.M.S., Cunha, P.P., 2014. Contaminated water, stream sediments and soils close to the abandoned Pinhal do Souto uranium mine, central Portugal. J. Geochem. Explor. 136, 102–117.
Pinto, M.M.S.C., Silva, M.M.V.G., Neiva, A.M.R., 2004. Pollution of water and stream sediments associated with the vale de abrutiga uranium mine, Central Portugal. Mine Water Environ. 23 (2), 66–75.
Poinssot, C., Geckeis, H., 2015. 3 - radionuclide behaviour in the natural environment: an overview. In: van Velzen, L. (Ed.), Environmental Remediation and Restoration of Contaminated Nuclear and Norm Sites. Woodhead Publishing, pp. 57–82.
Rihs, S., Condomines, M., 2002. An improved method for Ra isotope (226Ra, 228Ra, 224Ra) measurements by gamma spectrometry in natural waters: application to CO2-rich thermal waters from the French Massif Central. Chem. Geol. 182 (2), 409–421.
Rihs, S., Gaillard, C., Manceau, A., 2005. Interaction of U(VI) with birnessite: a solution chemistry and EXAFS study. Geochem. Cosmochim. Acta 69 (10). A627-A627.
Romer, R.L., Cuney, M., 2018. Phanerozoic uranium mineralization in Variscan Europe – more than 400 Ma of tectonic, supergene, and climate-controlled uranium redistribution. Ore Geol. Rev. 102, 474–504.
Rose, A.L., Waite, T.D., 2003. Kinetics of iron complexation by dissolved natural organic matter in coastal waters. Mar. Chem. 84 (1), 85–103.
Ryan, P.C., Hillier, S., Wall, A.J., 2008. Stepwise effects of the BCR sequential chemical extraction procedure on dissolution and metal release from common ferromagnesian clay minerals: a combined solution chemistry and X-ray powder diffraction study. Sci. Total Environ. 407 (1), 603–614.
Salbu, B., 2007. Speciation of radionuclides – analytical challenges within environmental impact and risk assessments. J. Environ. Radioact. 96 (1), 47–53.
Salbu, B., Burkitbaev, M., Strømman, G., Shishkov, I., Kayukov, P., Uralbekov, B., Rosseland, B.O., 2013. Environmental impact assessment of radionuclides and trace elements at the Kurday U mining site, Kazakhstan. J. Environ. Radioact. 123, 14–27.
Steinmann, M., Stille, P., 2008. Controls on transport and fractionation of the rare earth elements in stream water of a mixed basaltic–granitic catchment basin (Massif Central, France). Chem. Geol. 254 (1), 1–18.
Stewart, J.W.B., Cole, C.V., 1989. Influences of elemental interactions and pedogenic processes in organic matter dynamics. In: Clarholm, M., Bergström, L. (Eds.), Ecology of Arable Land — Perspectives and Challenges: Proceeding of an International Symposium, 9–12 June 1987 Swedish University of Agricultural Sciences. Springer Netherlands, Uppsala, Sweden, pp. 77–87. Dordrecht.
Štrok, M., Smodiš, B., Eler, K., 2011. Natural radionuclides in trees grown on a uranium mill tailings waste pile. Environ. Sci. Pollut. Res. 18 (5), 819–826.
Szalay, A., 1964. Cation exchange properties of humic acids and their importance in the geochemical enrichment of UO2++ and other cations. Geochem. Cosmochim. Acta 28 (10), 1605–1614.
Tessier, A., Campbell, P.G.C., Bisson, M., 1979. Sequential extraction procedure for the speciation of particulate trace metals. Anal. Chem. 51 (7), 844–851.
Tonkin, J.W., Balistrieri, L.S., Murray, J.W., 2004. Modeling sorption of divalent metal cations on hydrous manganese oxide using the diffuse double layer model. Appl. Geochem. 19 (1), 29–53.
Tournassat, C., Tinnacher, R.M., Grangeon, S., Davis, J.A., 2018. Modeling uranium(VI) adsorption onto montmorillonite under varying carbonate concentrations: a surface complexation model accounting for the spillover effect on surface potential. Geochem. Cosmochim. Acta 220, 291–308.
Villalobos, M., Bargar, J., Sposito, G., 2005. Mechanisms of Pb(II) sorption on a biogenic manganese oxide. Environ. Sci. Technol. 39 (2), 569–576.
WHO, 2004. Uranium in Drinking-Water: Background Document for Development of WHO Guidelines for Drinking-Water Quality. World Health Organization.
Williams, M., Fordyce, F., Paijitprapapon, A., Charoenchaisri, P., 1996. Arsenic contamination in surface drainage and groundwater in part of the southeast Asian tin belt, Nakhon Si Thammarat Province, southern Thailand. Environ. Geol. 27 (1), 16–33.
Zhu, Z., Zhu, M., Wu, Z., 2012. Pretreatment of sugarcane bagasse with NH4OH–H2O2 and ionic liquid for efficient hydrolysis and bioethanol production. Bioresour. Technol. 119, 199–207.